Magnetic Field and Tissue Dependencies of Human Brain Longitudinal ^1H_2O Relaxation in Vivo

William D. Rooney,[1,5*] Glyn Johnson,[2] Xin Li,[1,5] Eric R. Cohen,[3] Seong-Gi Kim,[3] Kamil Ugurbil,[3,6] and Charles S. Springer, Jr.[1,4,5]

Brain water proton (^1H_2O) longitudinal relaxation time constants (T_1) were obtained from three healthy individuals at magnetic field strengths (B_0) of 0.2 Tesla (T), 1.0T, 1.5T, 4.0T, and 7.0T. A 5-mm midventricular axial slice was sampled using a modified Look-Locker technique with 1.5 mm in-plane resolution, and 32 time points post-adiabatic inversion. The results confirmed that for most brain tissues, T_1 values increased by more than a factor of 3 between 0.2T and 7T, and over this range were well fitted by T_1 (s) = $0.583(B_0)^{0.382}$, T_1(s) = $0.857(B_0)^{0.376}$, and T_1(s) = $1.35(B_0)^{0.340}$ for white matter (WM), internal GM, and blood ^1H_2O, respectively. The ventricular cerebrospinal fluid (CSF) ^1H_2O T_1 value did not change with B_0, and its average value (standard deviation (SD)) across subjects and magnetic fields was 4.3 (±0.2) s. The tissue $1/T_1$ values at each field were well correlated with the macromolecular mass fraction, and to a lesser extent tissue iron content. The field-dependent increases in ^1H_2O T_1 values more than offset the well-known decrease in typical MRI contrast reagent (CR) relaxivity, and simulations predict that this leads to lower CR concentration detection thresholds with increased magnetic field. Magn Reson Med 57:308–318, 2007. © 2007 Wiley-Liss, Inc.

Key words: magnetic field; brain; tissue; relaxation; MRI

Developments in MRI have been characterized by continuous increases in the maximum strength of the magnetic field available for use. In Fig. 1 we extend the plot of the highest field strength (B_0, in Tesla (T)) employed as a function of the year in which the MR magnet was first demonstrated (1). Over most of the history of MRI, the relationship was nearly linear, indicating successful construction of, and a continued demand for, high-field systems. The solid-step function plots the U.S. Food and Drug Administration designation of nonsignificant risk device status, which now stands at 8T for adult human subjects. To be sure, the main forces driving the continued increase in magnetic field strength are the signal-to-noise ratio (SNR) and the increased resonant frequency dispersion. Significant improvements in both quantities with increasing magnetic field have been demonstrated (2,3). However, it is also important to investigate the field dependence of other NMR properties.

One of the important strengths of MRI is its ability to generate excellent soft-tissue contrast, and of particular interest is how MRI contrast depends on the magnetic field. For applications that require exceptional anatomical definition, T_1-weighted MRI is the preferred acquisition, and a longstanding concern has been the feared loss of T_1 contrast at high magnetic fields. It has long been known that tissue ^1H_2O relaxation time constants are field dependent (4).

It is generally understood that the increase of tissue ^1H_2O T_1 with B_0 is due to the simultaneous decrease of tissue spectral density at the Larmor frequency (5). The isothermal dependence of the longitudinal relaxation time constant (T_1) on B_0 is often termed "NMR dispersion" (NMRD), or sometimes "relaxometry." As was noted in a skeptical review (6), concerns had been expressed about an "anticipated convergence of T_1s" to larger values at high B_0, with a consequent loss of MRI contrast. Indeed, the extrapolation of an empirical fitting of low-field ex vivo data (7) would predict a convergence of the ^1H_2O T_1 values of white matter (WM) and gray matter (GM) at ~8T.

Though there have been many NMRD studies of ex vivo tissue samples and model solutions of macromolecules and macromolecular assemblies (4,8), one of the physical properties that is most difficult to mimic accurately (and is most sensitive to tissue state) is ^1H_2O relaxation. The wide range of human-sized magnet field strengths that are now available (Fig. 1) allows useful NMRD studies of tissue to be performed in vivo. We have developed techniques to accurately measure ^1H_2O T_1 in vivo with reasonable spatial resolution (9–11).

In this study we present data on the magnetic field and tissue dependencies of ^1H_2O T_1 in the human brain. This adds to the large body of primary literature regarding longitudinal relaxation behavior at a single B_0. T_1 determinations tend to have excellent intrastudy precision; however, like any measurement, they are sensitive to acquisition and processing details. In the current study we collected rigorous longitudinal relaxation data, using essentially identical acquisition and data-processing techniques, from the same cerebral image plane in each of several volun-

[1]Chemistry Department, Brookhaven National Laboratory, Upton, New York, USA.

[2]Department of Radiology, New York University, New York, New York, USA.

[3]Center for Magnetic Resonance Research, University of Minnesota, Minneapolis, Minnesota, USA.

[4]Department of Chemistry, State University of New York, Stony Brook, New York, USA.

[5]Advanced Imaging Research Center, Oregon Health and Science University, Portland, Oregon, USA.

[6]Max Planck Institute for Biological Cybernetics, Tübingen, Germany.

Grant sponsor: U.S. Department of Energy; Grant number: DE AC02–98CH10884; Grant sponsor: National Institutes of Health; Grant numbers: NS 40801; EB 00422; RR08079; EB 00331.

S.-G. Kim is now at the Department of Radiology, University of Pittsburgh, Pittsburgh, PA.

X. Li is now at the Advanced Imaging Research, Center, Oregon Health and Science University, Portland, OR.

C.S. Springer, Jr. is now at the Advanced Imaging Research Center, Oregon Health and Science University, Portland, OR.

*Correspondence to: William D. Rooney, Ph.D., Advanced Imaging Research Center (L452), Oregon Health and Science University, Portland, OR 97239. E-mail: rooneyw@ohsu.edu

Received 31 May 2005; revised 5 September 2006; accepted 22 September 2006.

DOI 10.1002/mrm.21122
Published online in Wiley InterScience (www.interscience.wiley.com).

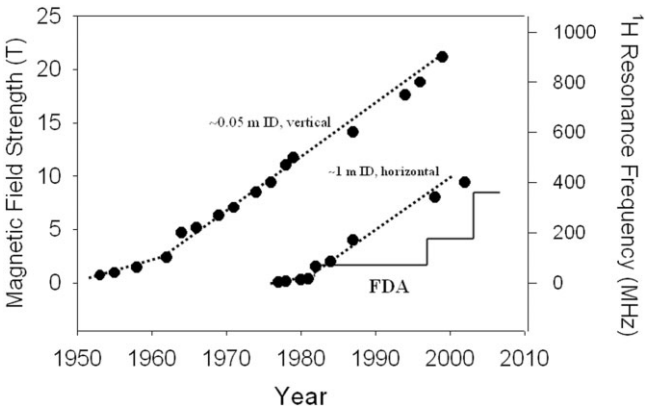

FIG. 1. Technological advances have led to continually increasing magnetic field strengths for NMR and MRI applications. The vertical axis is the B_0, in flux density (Tesla) on the left, and the corresponding ^{1}H resonance frequency ($\nu = \gamma B_0/2\pi$) on the right. The horizontal axis measures the year in which that field strength was first demonstrated. The upper filled circles represent magnets used for analytical NMR applications. The lower filled circles represent magnets suitable for the study of humans. The dotted lines are drawn to guide the eye. (This is an update of Fig. 2 in Ref. 1.) The solid step function represents the timeline of an FDA designation of nonsignificant risk device status.

teers at five B_0 values: 0.2T, 1.0T, 1.5T, 4.0T, and 7.0T. We validated our quantitative T_1 imaging technique using aqueous solutions with various paramagnetic compound concentrations and well characterized relaxation properties. We refer to the T_1 histograms found for living systems as longitudinal "relaxograms," and images made from discrete portions of these as "relaxographic images" (RIs). The latter constitute naturally T_1 segmented images (9). We further use the data to investigate the molecular bases of longitudinal relaxation in the human brain. Specifically, we estimate the relative contributions of macromolecules, iron, and contrast reagents (CRs) to in vivo ^1H_2O longitudinal relaxation. Finally, we explore the field dependence of in vivo longitudinal relaxation and discuss the implications for inherent contrast, and sensitivity for detecting CRs at high field.

MATERIALS AND METHODS

Three male volunteers between the ages of 32 to 59 years were studied on multiple MRI instruments with different B_0 values (0.2T, 1.0T, and 1.5T (all at New York University); 4.0T (at Brookhaven National Laboratory and the University of Minnesota); and 7.0T (at the University of Minnesota)) within a period of 6 months. All of the subjects provided informed consent prior to the study. Sagittal scout images of the head were obtained in order to select the same axial plane for each subject at each field strength. The scouts were gradient-recalled images with small TE values and 5-mm slice thickness. The axial slice chosen was a periventricular plane, oriented parallel to an imaginary line connecting the anterior and posterior commissures. This slice included the caudate nucleus, putamen, and thalamus structures. For relaxographic imaging of this slice, the progressively unsaturated relaxation during perturbed recovery from inversion (PURR) pulse sequence (9–12), a modified Look-Locker technique, was employed on each instrument. The inversion recovery (IR) was sampled at 32 times (τ) post-adiabatic inversion (13) using nonlinearly spaced delays ($0.02\ s \leq \tau \leq 10\ s$). The effective recycle time was 10.5 s. A low-flip-angle (nominally 5°) read pulse selected a 5-mm slice, and the $(192\ mm)^2$ FOV was encoded using a $(128)^2$ matrix. Thus, the 32 IR images had nominal in-plane and through-plane resolutions of 1.5 mm and 5 mm, respectively. All of the MRI data were reconstructed, and parametric maps were produced with the use of software developed in-house.

We investigated the accuracy of the PURR pulse sequence for the different MRI instruments using aqueous solutions containing various amounts of $NiCl_2$. The temperature and magnetic field dependencies of water proton relaxation properties in $NiCl_2$ solutions have been well characterized (14,15). Water proton T_1 values affected by Ni^{2+} show little dependence on temperature and magnetic field strength at approximately room temperature and for frequencies that are typical of MRI instruments, respectively. Because of these favorable properties, Ni^{2+} solutions are often used as calibration standards for quantitative relaxography (15). To determine the accuracy of the PURR imaging method, we used a spectroscopic T_1 measurement as a reference. For the latter, magnetization was inverted with the use of a hyperbolic secant pulse and residual transverse magnetization dephased with gradient pulses. A single inversion time was sampled for each 20-s recycle period. All measurements were performed at room temperature. Results from the PURR and spectroscopic measurements were compared with the use of linear regression.

To minimize field-dependent SNR differences, we set the readout gradient strengths, TEs, and total acquisition times to different values on the different instruments. The readout gradient strengths were 0.096, 0.153, 0.191, 0.51, and 1.11 G/cm for B_0 values of 0.2–7T, respectively. The TEs decreased from 11 ms at 0.2T to 4 ms at 7T. The total acquisition times were 90 min (four signal averages) at 0.2T, 45 min (two signal averages) at 1.0T, and 23 min for 1.5T, 4.0T, and 7.0T.

The signal dependence on inversion time, $S(\tau)$, for each image pixel was fitted with the three-parameter equation $S(\tau) = S_0(1 - b \cdot \exp(-\tau/T_1))$, using a minimization routine that employed a gradient expansion algorithm (S_0 is the signal intensity corresponding to the voxel Boltzmann equilibrium nuclear magnetization, and b is an empirical parameter that accounts for any imperfection in the voxel magnetization inversion). The resulting T_1 maps were coregistered with the use of Woods et al.'s (16) algorithm.

Regions of interest (ROIs) were manually selected from the following brain areas: a) frontal WM, b) putamen, c) caudate, d) thalamus, e) globus pallidus, f) frontal cortex, g) ventricular cerebral spinal fluid (CSF), and h) sagittal sinus (in order to obtain a measure of blood ^1H_2O T_1). The ROI volumes were approximately the same across subjects and field strengths for a given brain region. However, because of differences in local anatomy, and the desire to minimize partial-volume effects, there were differences in the ROI volumes sampled between brain regions. Typical ROI volumes were 30 mm^3 for the frontal cortex, globus

pallidus, and CSF; 180 mm^3 for internal GM (areas b–d); and 400 mm^3 for frontal WM. Since bilaterally symmetric regions were selected, the total tissue sampled for each subject for areas a–g was twice the values listed above. A single ROI within the sagittal sinus sampled approximately 30 mm^3 of blood.

For each subject, average T_1 values for the different brain areas were calculated from the ROI data. For regions a–f, the bilateral ROI pairs were averaged. For each B_0 value, data from the three subjects were averaged for each brain area. Descriptive statistics were calculated using the subject as the unit of measure. All data fittings were accomplished using a routine that employed a gradient expansion algorithm with chi-square minimization. Linear and nonlinear regression analyses were performed using SPSS software (SPSS Inc., Chicago, IL, USA).

RESULTS

We found excellent agreement between T_1 values extracted using the PURR and spectroscopic techniques, indicating that the imaging technique provided excellent accuracy. Linear regression returned an average slope of 1.00 (±0.04), intercept of 0.00 (±0.09), and $r^2 > 0.99$. T_1 values for the $NiCl_2$ solutions extracted using the PURR pulse sequence indicated no magnetic field dependence from 0.2T to 1.5T, and only a modest increase for 4T and 7T. The dependence of ^1H_2O R_1 [$\equiv(T_1)^{-1}$] values on Ni^{2+} concentration can be used to calculate the aqueous Ni^{2+} relaxivity (r_{1Ni}), which facilitates comparison with literature values. From our phantom data we estimate r_{1Ni} to be 0.63 (± 0.02) s^{-1}/mM from 0.2T to 1.5T, and 0.71 (± 0.03) s^{-1}/mM and 0.93 (± 0.23) s^{-1}/mM at 4T and 7T, respectively. Our results are in excellent agreement with literature values (14,15). Kraft and coworkers' (15) found that aqueous Ni^{2+} relaxivity was field-independent between 0.02T and 2.3T (1–100 MHz) at 0.62 (± 0.02) s^{-1}/mM, and 0.89 s^{-1}/mM at 6.3 T (270 MHz). In Fig. 2a we plot the field dependence of the aqueous Ni^{2+} relaxivity calculated from our data (diamond-shaped symbols) and literature values (square symbols (14,15)).

In Fig. 2b we plot 4T T_1 relaxograms obtained from essentially the same axial brain slice of the same 59-year-old subject collected on instruments at different institutions and 6 months apart. We constructed the T_1 distributions of Fig. 2b (and throughout) by binning and summing the individual voxel T_1 values from the entire slice. We refer to these as "composite" relaxograms (9). The associated T_1 maps of the Fig. 2b relaxograms are displayed as insets. The agreement between the T_1 relaxograms is excellent, as can be seen by the near-perfect alignments of the low T_1 relaxographic edge and other fine-structure details. Although the slice repositioning is quite good, it is not exact, and this is reflected in different frequency values for the T_1 bins. This emphasizes the importance of using consistent acquisition and processing techniques to minimize T_1 variability (see below).

The 32 IR images at each field strength are shown for one subject (32 years old) in the left column of Fig. 3. The τ matrix is the same in each panel (0.02 s at upper left, 10 s at lower right). It is very obvious that the minimum signal intensity of brain parenchyma occurs at an increasing τ value as B_0 increases. Therefore, for a given IR time (τ), one obtains very different contrast depending on the value of B_0 used. As an example, the right column shows the τ = 535 ms IR magnitude images (of the same subject). The relative contrast (defined here as the difference in signal magnitudes between the putamen and WM, normalized to CSF intensity) is −0.28, −0.26, 0.02, 0.22, and 0.18 going from 0.2T to 7T. This example of a sign reversal in relative contrast between these structures clearly emphasizes the need for sequence optimization at each field strength in order to achieve the desired contrast.

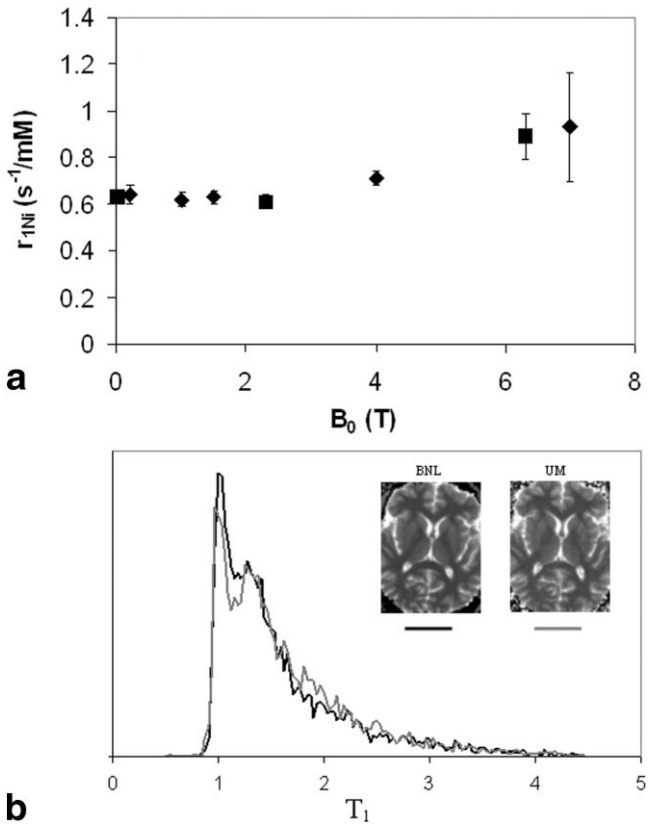

FIG. 2. **a:** The relaxivity (r_{1Ni}) of a $NiCl_{2,aq}$ solution as a function of B_0 at room temperature. The data from the current study are indicated by filled diamonds, and literature values (14,15) are indicated by filled squares. The error bars represent the measurement SD. **b:** Brain 4T T_1 relaxograms collected from a 59-year-old male at different institutions and 6 months apart (insets show the associated T_1 maps).

One way to display longitudinal relaxographic imaging data is to use a T_1 map (9). On such a map the pixel intensity is made proportional to the voxel ^1H_2O T_1 value. The T_1 maps for the same subject at the five fields are shown at the top of Fig. 4. An annotated grayscale is displayed at the lower right corner of the top panel. The intensities are rendered on the same grayscale; therefore, the images become brighter as one moves from 0.2T to 7.0T, indicating that brain parenchymal T_1 values are all increasing. To illustrate some of the spatial changes that occur in brain ^1H_2O T_1 values, we attempted to choose the same representative profile in each T_1 map. This is shown as a white line moving radially outward from a position in

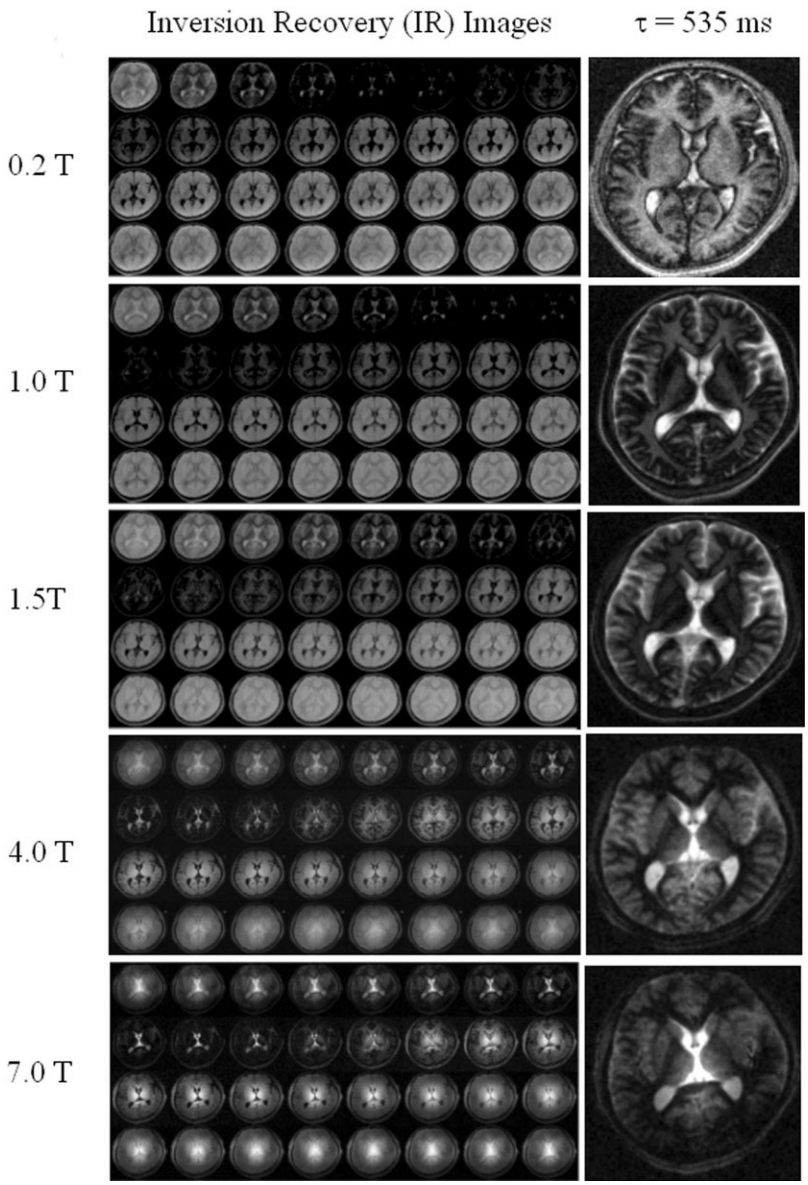

FIG. 3. The 32 IR images obtained for one subject at each field strength are shown in the left column. The recovery times range from 0.02 s at the upper left to 10 s at the lower right of each set. Magnitude images are displayed, so overall image intensity is high for small and large τ values and goes through a minimum based on the tissue T_1 values. Since the average tissue T_1 value increases with B_0, the apparent signal intensity minimum shifts to higher τ values as B_0 increases. In the right column, τ = 535 ms IR images are shown for each B_0, with constant grayscale. Contrast between GM and WM changes markedly with B_0, emphasizing the need to properly adjust sequence parameters at each B_0 to optimize tissue contrast. The effects of RF inhomogeneity are also clear for the 4T and 7T images, which tend to show increased signal intensity at the image center.

the thalamus, through internal capsule WM, globus pallidus, putamen, and finally into cortical GM just shy of the subarachnoid CSF. A stacked plot of the intensities along these profiles is presented at the bottom of Fig. 4. The origin of the abscissa corresponds to the origin of the profile in the thalamus, and the right side corresponds to the cortical GM terminus (units in millimeters, ordinate units in milliseconds). It is evident that peaks representing the cortical and internal GM structures are clearly defined at all fields, indicating that T_1 contrast between these structures is maintained at high fields.

Another way to present relaxation data is to display the RIs themselves (9). Two of these are shown in Fig. 5 superimposed on a stacked plot of the whole-slice relaxograms of the same subject as in Fig. 3. Here the abscissa is T_1 (in seconds) and the vertical offset is linearly proportional to the value of B_0. The local ordinate scales are normalized such that the total area under each relaxogram is constant. The 1.5T GM and 4.0T WM RIs are displayed. The integration limits (i.e., T_1 range) used to create these images are demarcated by the aqua- and olive-colored regions, respectively, in every relaxogram. It is clear that tissue ^1H_2O T_1 increases with increasing B_0, since the median value of the distribution moves to higher T_1 with a hyperbolic trajectory. However, what is evident in the plots, although not universally anticipated, is that the distribution of parenchymal T_1 values also broadens with increasing field. At the far right of each relaxogram, a peak is inserted to indicate the T_1 distribution of CSF ^1H_2O, which is essentially B_0-independent.

The field dependence of the T_1 values is further illustrated in Table 1 and Fig. 6, in which data from all three subjects are pooled. The data from the current study are indicated by bold entries in Table 1 at 0.2T, 1.0T, 1.5T, 4T, and 7T. The group-averaged ^1H_2O T_1 values from specific ROIs in frontal WM, globus pallidus, putamen GM, thalamus GM, sagittal sinus blood, and lateral ventricle CSF were calculated. The data for the frontal WM, putamen

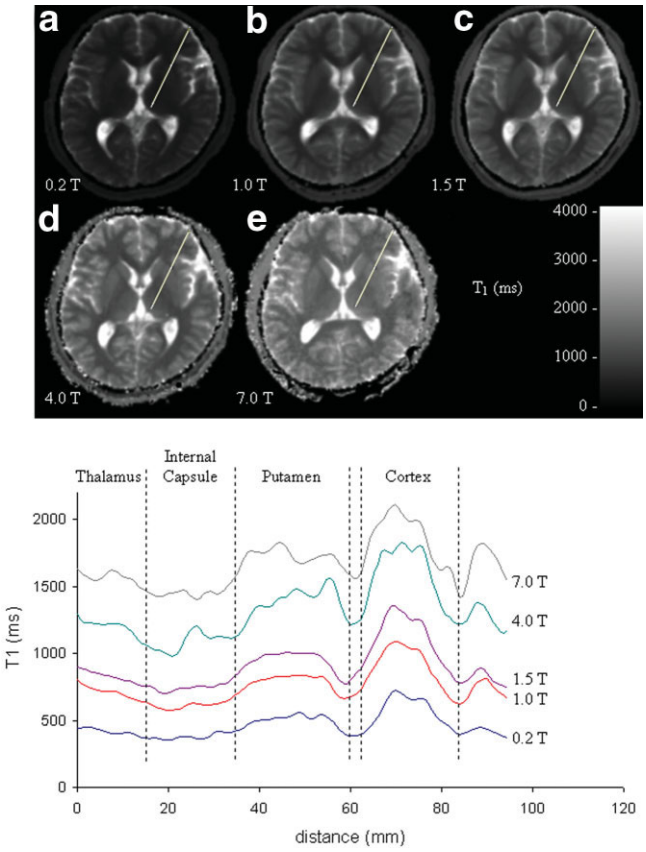

FIG. 4. The brain-tissue B_0 dependence of T_1 is illustrated. The T_1 maps for the Fig 3 subject at each B_0 are displayed at the top, where the pixel signal intensity, on the same grayscale, is proportional to its T_1 value and is indicated by the scale at the lower right. The T_1 maps were coregistered using Woods et al.'s (16) AIR program. The line plots at the bottom display T_1 profiles along the white lines that radiate diagonally from the thalamus to the cortex in each of the T_1 maps.

GM, and sagittal sinus blood are illustrated in Fig. 6 with circle, square, and diamond symbols, respectively. The error bars represent the intersubject standard deviations (SDs). The solid curves in Fig. 6 represent fittings with Bottomley et al.'s (17) function: $T_1 = C(\gamma B_0)^{\beta}$, where γ is the magnetogyric ratio, and B_0 is in Tesla. The best fittings obtained are given by T_1 (s) $= 0.00071(\gamma B_0)^{0.382}$, T_1(s) $= 0.00116(\gamma B_0)^{0.376}$, and T_1(s) $= 0.00335(\gamma B_0)^{0.340}$ for WM, putamen GM, and sagittal sinus blood data, respectively. Although these two-parameter functions are completely empirical in nature, they are concise and useful for interpolating/extrapolating T_1 behavior over typical magnetic field strengths for human MRI instruments. However, at high or low magnetic field strengths, the predictions are physically unreasonable. This suggests that more than two parameters are necessary for modeling over a larger frequency range. Extrapolations from low-field data predicted a coalescence of WM and GM T_1 values near 8T (7). Clearly, the experimental data shown in Fig. 6 are still diverging at 7T.

Consistent with in vitro literature reports, we found a significant increase of blood ^1H_2O T_1 values with B_0. Increased blood T_1 can have important consequences for many MRI studies, but particularly for spin-labeled perfusion MRI. However, a complication for in vivo (as opposed to in vitro) blood ^1H_2O T_1 measurements is that they are potentially affected by flow (18). Flow-related errors in

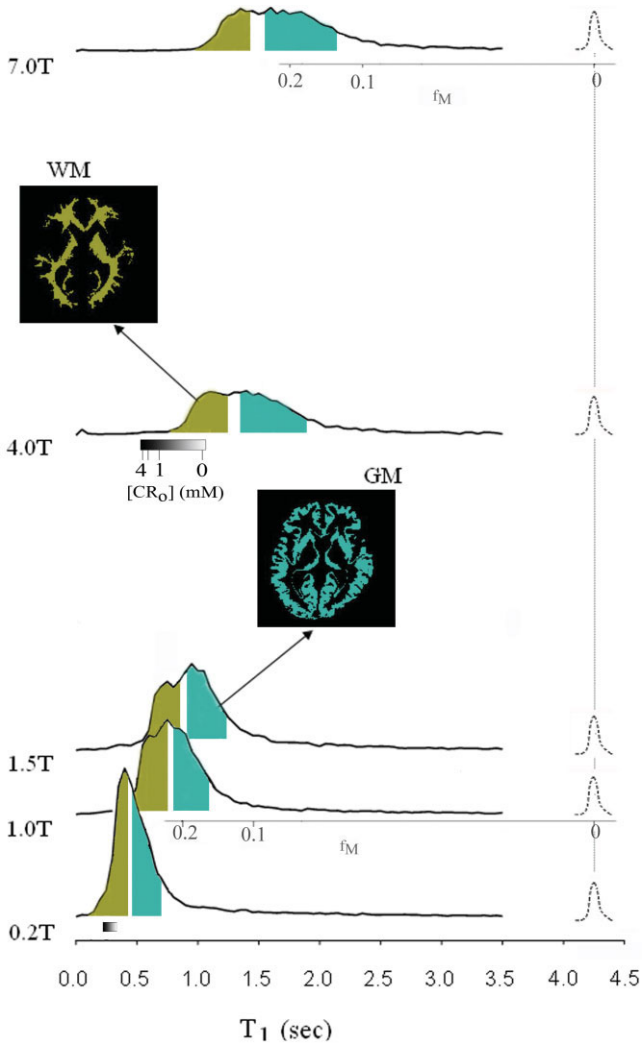

FIG. 5. Stacked plot of the brain-slice T_1 relaxograms from data shown in Figs. 3 and 4. The horizontal axis measures the T_1 value, and each local vertical axis is proportional to the number of voxels. The stacked plot vertical offset is proportional to B_0. The distribution median value shifts to higher T_1 and its width increases with B_0. A sharp peak is inserted at 4.3 s to indicate the position of CSF at 37°C. Its T_1 value is B_0-independent. The 4.3-s peak width indicates the estimated between-subject variance of the measure. The colored regions in each relaxogram demarcate integration limits that produce RIs with essentially identical spatial distributions. An example, a 4T RI with integration limits selected to show WM is displayed between the 4T and 7T relaxograms. A 1.5T RI for GM is displayed between the 1.5T and 4.0T relaxograms. These RIs have been masked to remove extracranial signals, and effectively provide the spatial extent of WM and GM. The integration limit ranges required to produce homologous RIs increase with B_0. The f_M axis under the 1.0T and 7.0T relaxograms measures the tissue macromolecular volume fraction. The nonlinear grayscale bars under the 0.2T and 4T relaxograms indicate the expected [CR_o]-dependent WM ^1H_2O T_1 shifts caused by the presence of an extracellular CR at concentrations from 0 (white) to 4 (black) mM. (See text for comment.)

Table 1
Mean Regional Brain ^1H_2O T_1 Values (±SD)*

B_0 (T)	WM	cGM	Caudate	Thalamus	Putamen	Globus pallidus	Blood	CSF	Reference
0.15	352 (±39)							4360 (±600)	20, 21
0.20	**361 (±17)**	**635 (±54)**	**555 (±19)**	**522 (±44)**	**524 (±19)**	**411 (±20)**	**776 (±22)**	**4408 (±187)**	**This study**
0.50	366 (±11)								22
0.60								4220 (±280)	20
1.0	**555 (±20)**	**1036 (±19)**	**898 (±45)**	**807 (±47)**	**815 (±16)**	**625 (±14)**	**1351 (±24)**	**4276 (±109)**	**This study**
1.5	**656 (±16)**	**1188 (±69)**	**1083 (±52)**	**972 (±32)**	**981 (±13)**	**746 (±20)**	**1540 (±23)**	**4070 (±65)**	**This study**
1.5	633 (±8)	1148 (±24)						5127 (±350)	23
	636 (±29)	1113 (±48)		814 (±26)	919 (±42)				24
	641 (±11)	1085 (±31)	1080(±20)	850 (±23)	953 (±22)				25[b]
1.6								4310 (±520)	20
3.0	838 (±78)	1283 (±161)							26
	847 (±43)	1763 (±60)	1483(±42)	1218 (±40)	1337 (±42)				27
4.0	**1010 (±19)**	**1723 (±93)**	**1509 (±53)**	**1452 (±87)**	**1446 (±32)**	**1143 (±27)**	**1914 (±114)**	**4472 (±85)**	**This study**
4.0	1043(±27)	1724 (±51)	1458(±37)		1372 (±60)			4550 (±800)	28
	831 (±37)	1311 (±66)	1520(±90)	1214 (±72)	1271 (±81)			3386 (±460)	30[a]
	1010 (±60)	1530 (±70)		1350 (±50)	1320 (±40)			3500 (±400)	10
7.0	**1220 (±36)**	**2132 (±103)**	**1745 (±64)**	**1656 (±84)**	**1700 (±66)**	**1347 (±52)**	**2587 (±283)**	**4425 (±137)**	**This study**

*All values are in milliseconds.
[a]4.1 T.
[b]Right side brain T_1 values.

these measurements could be magnetic field-dependent because of the blood ^1H_2O T_1 increase with B_0. For the measurements reported here, we used a nonselective adiabatic inversion that because of the coil geometry had an effective slice thickness of about 20 cm. The low-flip-angle read pulse was applied with gradients and had a slice thickness of 5 mm. The effective flip angle at the sagittal sinus was even lower than its nominal value for the 4T and 7T measurements, since data collected from these instruments have RF center-peripheral power roll-offs of about 1 dB and 3 dB, respectively (2), and the flip angle was adjusted to its nominal value at the brain center. Therefore, even though the larger ^1H_2O T_1 value associated with larger B_0 increases potential in-flow effects, the effectively lower flip angle of the high-field systems tends to mitigate any systematic flow differences. Bryant and coworkers (19) reported properties of blood ^1H_2O R_1, measured ex vivo at 297 K, over the υ_0 range of 0.01–60 MHz. We also fitted the blood data of Fig. 6 using Bryant et al.'s (19) equation: $T_1 = \{A^2\,\tau_c\,\{[1/(1+(\omega_0\tau_c)^\beta)] + [4/(1+(2\omega_0\tau_c)^\beta)]\}^{-1}$, with $A^2 = 8.68 \times 10^6\ s^{-2}$, $\tau_c = 1.0 \times 10^{-7}$ s, and $\beta = 0.4$. The fitting was essentially identical to that indicated by the solid line in Fig. 6. We fixed A^2 at Bryant et al.'s value (this assumes that the dipolar coupling is temperature-independent and that the temperature dependence arises from the τ_c parameter). Bryant et al. obtained $\tau_c = 1.8 \times 10^{-7}$ s and $\beta = 1.0$ for the field dependence of whole blood ex vivo at 297 K. The reduced τ_c value we obtain at physiological temperature is consistent with a thermally activated process with an activation energy of 34 kJ/K · mole.

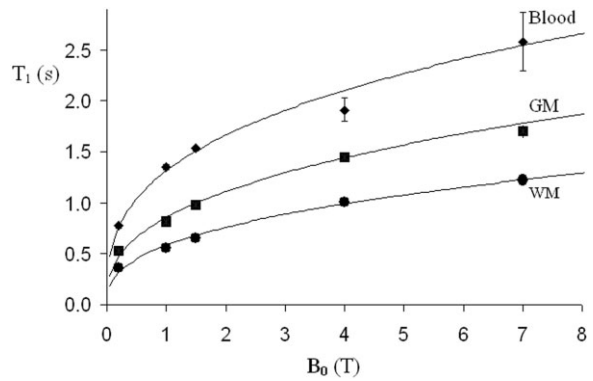

FIG. 6. B_0-dependence of the mean GM and WM ^1H_2O T_1 values. The squares, circles, and diamonds represent group-averaged T_1 data obtained from putamen, frontal WM, and sagittal sinus ROIs, respectively. The error bars represent 1 SD of the group mean T_1 values. The error bars are about the same size as the symbols, for most data points. The solid curves represent the best fittings of the empirical function $T_1 = C(\gamma B_0)^\beta$. See text for details.

The ventricular CSF ^1H_2O R_1 values we obtain do not vary with B_0 (Table 1) and average 0.231 (± 0.009) s^{-1}. This finding is consistent with and extends the results of Hopkins and coworkers (20), who reported human CSF H_2O R_1 values of 0.233 (± 0.004) s^{-1} for B_0 of 0.15T, 0.6 T, and 1.4T. A potential problem in sampling CSF is partial-volume contamination by surrounding tissue. This would tend to reduce extracted T_1 values, which was likely an issue in one of our earlier studies (10) that used a lower-resolution acquisition.

DISCUSSION

In this study we determined brain ^1H_2O longitudinal relaxation time constant distributions for three healthy individuals studied at five different B_0 values ranging from 0.2T to 7.0T. The use of the same volunteers and essentially identical acquisition and processing techniques for each data set minimizes variability due to biological and technical issues. The T_1 values we obtained at $B_0 \leq 4$T are in good agreement with previously reported results (10,21–30), some of which are listed in Table 1. While the

T_1 intrastudy measurement precision was sometimes excellent, the agreement between studies performed on different instruments was often poor. Examples of this can be seen in the Table 1 entries. The interstudy variability of the 4T WM data was 22%, even though the intrastudy variability was relatively small (no more than 6%).

Our results clearly show a continuous increase not only in the brain tissue ^1H_2O T_1 values with B_0, but also in their intertissue distribution widths. These findings can be interpreted on a molecular basis. Fortunately, in contrast to the case with transverse relaxation, T_1 is readily amenable to such analytical interpretations. The variation in tissue ^1H_2O R_1 values at any given B_0 can be empirically modeled using the following equation:

$$R_1 = R_1' + r_{1M}f_M + r_{1Fe}[Fe] + r_{1CR}[CR] \quad [1]$$

where R_1' is the value for pure saline (at physiological temperature), and r_{1M}, r_{1Fe}, and r_{1CR} are the macromolecular site, iron site, and CR relaxivities, respectively. In principle, each relaxivity could be further indexed for brain region or tissue subtype. The concentration of macromolecular sites is proportional to the macromolecular mass fraction, f_M (the macromolecular volume fraction, if the density is taken as unity). Thus, we can define r_{1M} as the relaxivity per unit macromolecular mass fraction, and [Fe] and [CR] as the effective concentrations of iron and CR, respectively. (The quantity r_{1CR} is traditionally symbolized simply as r_1, but we are more specific in the present context.) An assumption inherent in Eq. [1] is that fast-exchange-limit (FXL) conditions (on the T_1 time scale) apply for water interchange between all sites. That is, within a given measurement volume, water can sample all possible equivalent sites with exchange rate constants that are much greater than the differences in site-associated R_1 values (31).

The relaxivity for component "X" (where X represents a macromolecular, iron, or CR site) can be written as

$$r_{1X} = K_{f,X}\{< R_{1b,X} > - R_1'\} \quad [2]$$

where $K_{f,X}$ is a constant that includes the apparent formation constant for the water–X interaction and unit conversion constants if necessary. The $R_{1b,X}$ term represents the average effective ^1H_2O longitudinal relaxation rate constant associated with all microscopic sites of component X. It is important to appreciate that the water interaction at any microscopic site can involve both water molecular exchange and proton exchange, although proton exchange at typical physiological conditions is likely to be slow compared to molecular exchange. The quantity $|R_{1b,X} - R_1'|$ is the longitudinal relaxographic NMR shutter speed for exchange (31). It is generally small for macromolecules (8), but has the potential to be important for some sites, particularly at low magnetic field. It is also important to realize that the B_0 dependence of r_{1X}, and thus R_1, enters through the $R_{1b,X}$ term.

A number of studies with excised tissue samples have demonstrated the validity of the second term on the right hand side (RHS) of Eq. [1] (32–35); however, in many of these studies the abscissal variable was chosen as $(1 - f_M)^{-1}$ [$\equiv f_w^{-1}$]. The success of linear f_M or $(1 - f_M)^{-1}$ plots in these cases is evidence that the equilibrium system, between free water and macromolecule-interacting water, is in the FXL (31,33). Gelman and coworkers (26) published a $(1 - f_M)^{-1}$ plot for in vivo human MRI data. However, it is also important to consider contributions from intrinsic paramagnetic compounds, which in the normal brain are dominated by iron(III) complexes.

The significance of the third term (r_{1Fe}[Fe]) on the RHS of Eq. [1] was argued by Ogg and Steen (36) based on in vivo relaxography and analyses of postmortem tissue samples for iron content. However, a confounding aspect arises because both tissue f_M and [Fe] strongly covary, especially in the developing brain (37). Rigorous analyses by our group and others (26) suggest that the third term on the RHS of Eq. [1] is less important than the second term, and that spatial differences in macromolecular volume fraction can explain most of the spatial T_1 variance in normal brain. Brain iron is stored almost exclusively in ferritin-like proteins, and iron in these structures is typically not very efficient in catalyzing ^1H_2O longitudinal relaxation. Gossuin et al. (38) measured the longitudinal relaxation rate constant of ^1H_2O in neutral ferritin solutions from 0.02 MHz to 500 MHz at 37°C. From their data we estimate that r_{1Fe} decreases slightly with B_0 from 0.04 s^{-1}/mM Fe at 0.2T to 0.03 s^{-1}/mM Fe at 7T. For comparison, this iron relaxivity is more than 100 times less potent than typical low-molecular-weight gadolinium (Gd)-based CRs. The iron content of adult human brain tissue ranges from 0.01 mg/g to 0.21 mg/g (37), corresponding to effective tissue water iron concentrations of ~0.2 mM to 5.3 mM. Using the 4T r_{1Fe} and the average normal adult thalamus concentration of 0.048 mg Fe/g tissue (1.2 mM Fe) (37), we estimate a value for the third term on the RHS of Eq. [1] (r_{1Fe}[Fe]) to be 0.037 s^{-1}. This represents about 5% of the thalamus ^1H_2O R_1 value measured at 4T, but can be more than 20% of total R_1 for high-iron-content structures, such as the globus pallidus (see below). In comparison, transverse relaxation processes do not require actual molecular interaction, and stored iron can be a significant determinant of T_2 and T_2^* values (38). Although the absolute R_1 iron contribution decreases slightly with increasing B_0 (38), its relative contribution in vivo is expected to increase, which could lead to improved iron R_1 quantification at higher magnetic fields.

From our results we were able to estimate the relative contributions of r_{1M} and r_{1Fe} in determining tissue ^1H_2O longitudinal relaxation. The T_1 values we obtained (bold entries Table 1) were reciprocated, and for each tissue ROI we subtracted the CSF R_1 value to obtain an excess R_1 (i.e., $R_1 - R_{1,CSF}$). The brain tissue ^1H_2O excess R_1 values are plotted against the macromolecular mass fraction (f_M) in Fig. 7. To first approximation, all of the excess R_1 variance can be attributed to tissue macromolecular content. The linear regressions, with each regression using r_{1M} as the only variable, are shown in Fig. 7a. It is important to note that the ordinate (R_1 from this work) and abscissa (f_M from Refs. 26, 35, and 39) measurements are completely independent. Although the fittings are quite reasonable ($r^2 > 0.9$), some systematic discrepancies are apparent across all B_0 values. For example, the ^1H_2O R_1 values of thalamus (at $f_M = 0.250$; [Fe] = 1.17 mM) fall below the regression

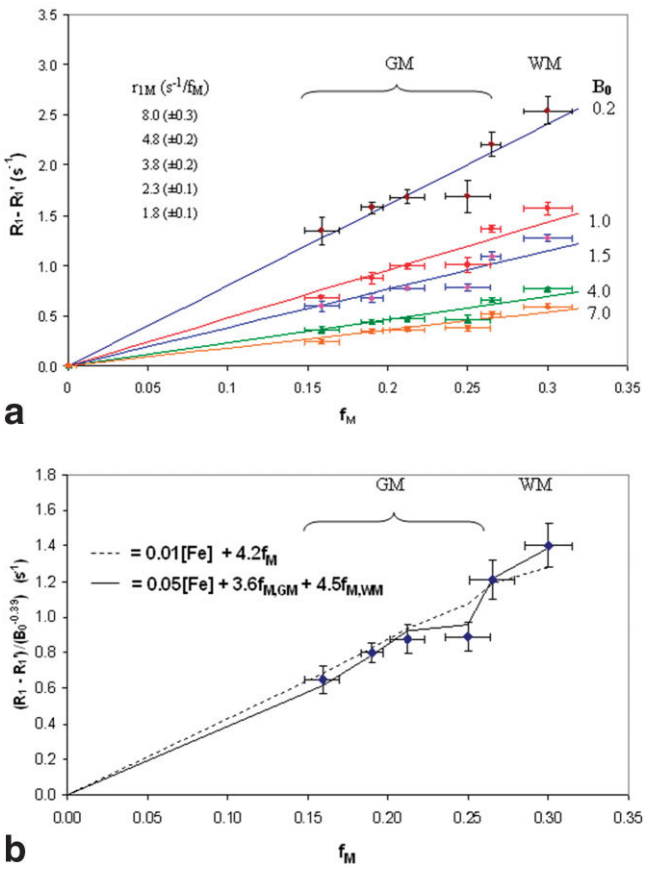

FIG. 7. **a:** Brain ^1H_2O R_1 data from different B_0 values plotted against tissue macromolecular mass fraction, f_M. The symbols represent average R_1 values obtained from three subjects (see Table 1), after subtracting $R_{1,CSF}$ (i.e., excess tissue R_1 values), and the f_M values were obtained from the literature (39). The error bars measure SDs. The solid lines represent linear regressions, and slopes (r_{1M} values) are indicated as inserted text. **b:** Average tissue excess R_1 values following normalization to B_0 = 1T (i.e., dividing each R_1 by $(B_0)^{-0.39}$). The lines were obtained by fitting the data using a model with two parameters (r_{1M}, and r_{1Fe}; dotted line) or three parameters ($r_{1M,GM}$, $r_{1M,WM}$, and r_{1Fe}; solid line). The solid line has a significantly better fit to the data, suggesting that the regional variation in brain iron content explains the nonlinearity in the plot. The expressions for the dotted and solid lines are indicated as inserted text.

lines, while the R_1 values of globus pallidus (at f_M = 0.265; [Fe] = 5.30 mM) and frontal WM (at f_M = 0.305; [Fe] = 1.14 mM) are all above the regression lines. This residual autocorrelation suggests that a single variable regression is insufficient, and that one or more additional parameters are required.

To more closely examine the fine structure present in the Fig. 7a plots (particularly the discontinuity for the thalamus at f_M = 0.25), we averaged the excess R_1 values after removing their B_0 dependence. We accomplished this by dividing the excess R_1 data by $(B_0)^{-0.39}$, essentially normalizing all data to a field of 1T. We determined the power function exponent by nonlinear regression using all tissue excess R_1 data against B_0. We then averaged the transformed R_1 data for each tissue ROI. The results are plotted in Fig. 7b (error bars indicate the SDs). We modeled these results with the second two RHS terms of Eq. [1], using literature f_M (26,35,39) and [Fe] (37) average values. The fitting returned values of 4.22 (±0.17) s^{-1}/f_M and 0.014(±0.014) s^{-1}/mM Fe for the macromolecular and iron relaxivities, respectively. The predicted function is plotted as a dotted line in Fig. 7b. Systematic deviations between the model and the data are still clearly evident, particularly for thalamus (f_M = 0.25) and WM data points.

As stated above, macromolecular relaxivity can differ for each tissue subtype. The next most parsimonious approach is to allow GM and WM r_{1M} values to differ, since these tissue subtypes are known to have different chemical compositions and morphologies, which can result in different macromolecular relaxivities. The result for the three-parameter regression (r_{1Fe}, $r_{1M,GM}$, $r_{1M,WM}$) is plotted as a solid line in Fig. 7b. It clearly reproduces the fine structure expressed in the R_1 data. The major discontinuities in the Fig. 7 plots can be explained by [Fe] differences between GM structures. The discontinuity is most evident between the thalamus (a low-iron-content region) and the globus pallidus (a high-iron-content region). The parameters returned from the fitting are 3.64 (±0.17) s^{-1}/f_M for $r_{1M,GM}$, 4.53 (±0.17) s^{-1}/f_M for $r_{1M,WM}$, and 0.047 (±0.012) s^{-1}/mM Fe for r_{1Fe}. All are significant predictors of brain ^1H_2O R_1 values. Moreover, the r_{1Fe} value we obtained is in good agreement with that reported for in vitro ferritin by Gossuin et al. (38).

For illustrative purposes, we added an f_M scale to the 1.0T and 7.0T relaxogram abscissae in Fig. 5. We did this by letting f_M be 0.3 for WM and 0.2 for GM (39), and placing those abscissal values at the centers of the WM and GM distributions, respectively. Since f_M is linear in R_1 (Eq. [1]), this results in a nonlinear scale for T_1, since the 0.10 f_M value is in the mid-region of the broad (partial volumed) CSF shoulder. A sharp relaxographic peak representing CSF is sketched at 4.3 s on each relaxogram. This represents the situation in which f_M is nearly zero. Since the T_1 of CSF ^1H_2O is not field-dependent (4,20) (Table 1), we connected the peaks at each of the fields with a dotted vertical line. The idea here is that, to first approximation, in vivo longitudinal relaxograms can be thought of as mostly f_M measures.

To complete our discussion of tissue ^1H_2O R_1 determinants, it is important to briefly return to CRs, since their use is pervasive in MRI, and the field dependence of both r_{1CR} and r_{1M} impacts CR detection sensitivity. It is clear from Fig. 5 that increasing B_0 causes shifts to the right in longitudinal relaxographic space. On the other hand, since an MRI CR is a relaxation catalyst, it acts to shift such peaks to the left (12,31). This represents a synergistic relationship. Again for illustrative purposes, we added extracellular CR concentration, $[CR_o]$, scales to the 4T and 0.2T relaxogram abscissae in Fig. 5, using appropriate cell-free saline values (40) for r_{1CR} at the two fields. A linear expression between tissue R_1 and [CR] is generally not appropriate for the in vivo situation. This is because the CR distributes at most into the extracellular spaces, while most of the tissue water is intracellular. Equilibrium transcytolemmal water exchange does not occur frequently enough for the FXL condition to be maintained at moderate to high $[CR_o]$ (31). Effectively, this renders r_{1CR} dependent on $[CR_o]$, and this has been taken into account in the Fig. 5 $[CR_o]$ scales (shown as grayscale bars, with

white for 0 mM and black for 4 mM). We placed the zero $[CR_o]$ value in the center of the WM water distribution in each case. This is arbitrary, because CR presence in any tissue can cause the shift of its ^1H_2O T_1 peak. Since T_1 cannot be negative (it is the reciprocal of a rate constant, R_1), it is clear that the $[CR_o]$ scale is quite compressed at low field strengths. On the other hand, it is expanded at high fields, particularly for the lowest $[CR_o]$ values. The illustration with WM water is conservative, and the expansion would be even greater for GM water. This accounts for the qualitative observation that a given CR dose causes increased image enhancement at higher field (41). We previously showed (31) that the combination of this increased sensitivity to low [CR] values at high fields and the increased SNR at high fields leads to an increased likelihood of actually remaining in the FXL condition, which simplifies the analysis considerably, and which is always (inappropriately) assumed at clinical field strengths. Even more importantly, it leads to the result that the detection threshold [CR] value *decreases* with increasing B_0 (42,43). One can quantify this effect by realizing that the CR detection sensitivity, s_{CR}, depends on the relative change in tissue ^1H_2O R_1 when CR is present, i.e.,

$$s_{CR} = \Delta R_1/R_{10} = r_{1CR}[CR]/R_{10} \quad [3]$$

$$ds_{CR}/dB_0 = d(r_{1CR}/R_{10})/dB_0 \quad [4]$$

The cell-free value of r_{1CR} for $GdDTPA^{2-}$ decreases only 30% (from 5.2 to 3.6 s^{-1}/mM) (40) between 0.2T and 7T, while WM ^1H_2O R_1 values decrease by more than 70%. The net effect is a more than twofold increase in s_{CR} due to relaxation effects alone. B_0-dependent SNR increases further increase the CR detection sensitivity.

SNR and contrast-to-noise ratios (CNRs) are important metrics of overall image quality, and a longstanding concern is the potential loss of T_1 contrast with increasing B_0. Based on the T_1 values we obtained, the relative contrast between GM and WM that is attainable in a spoiled gradient-recalled-echo sequence is essentially field-independent, decreasing by less than 6% from 0.2T to 7T. An additional and important consideration is the effect of increased T_1 values on the SNR. Although a nominal SNR is expected to increase linearly with magnetic field (2), this does not take into account the effect of increased T_1 in repetitive pulse experiments. In the latter the expected linear increase in SNR with B_0 will be mitigated because of increased signal saturation for a given TR value. Alternatively, to maintain saturation factors (and desired T_1-weighted contrast) with increasing B_0 for a given flip angle, one must increase the TR values commensurately with the T_1 increases, which results in a reduced signal-averaging capability. However, the rate of T_1 increase with B_0 is hyperbolic and falls with increasing B_0 (Fig. 6). Therefore, the relative T_1-associated SNR penalty with increasing field is much worse at low B_0, where dT_1/dB_0 is much greater than at high B_0 (Fig. 6). Most of this penalty is incurred by 1.5T. The effective SNR penalty due to increased T_1 essentially scales with the square root of the T_1 ratio between fields, roughly a factor of 1.7 between 0.2 and 7T. So instead of a factor of 35, the expected SNR increase of a standard T_1-weighted acquisition is approximately 20. To summarize, we find that GM/WM T_1 contrast is essentially field-independent; however, achieving this contrast necessitates a selective saturation of spins, which results in an SNR increase that is somewhat less than linear with B_0. Therefore, we expect the CNR between GM and WM structures to increase substantially with B_0. We previously showed that excellent natural segmentation of human brain images can be achieved at 4T (30).

This study has several limitations, primarily related to the small number of subjects studied. Our focus here was to investigate the magnetic field dependence of T_1, and we limited the study to only men between the ages of 32–59 years. Since the T_1 changes with B_0 we studied are much larger than intersubject variability (see Table 1), and effect sizes are always greater than 5, this objective could be realized with a small number of subjects. However, an inherent limitation of such a small subject group is that intersubject variability estimates for any given brain region can be biased high or low. An inspection of the Table 1 entries makes it clear that the precision of any given literature study is quite good: on average, the intersubject normalized variance is just over 4%. On average, our intersubject variability estimates are consistent with these results. The remarkable constancy of T_1 intersubject variability across studies, time, and a wide range of magnetic field strengths suggests that measurement uncertainties are likely dominated by biological variability. We (30) and other investigators (27) have found that brain ^1H_2O T_1 values differ between the sexes and increase with age. Since our study subjects were all men less than 60 years old, a second limitation is that we did not gain any insight into how the B_0 dependence of brain water proton T_1 might differ with age and sex.

Despite these limitations, it is clear that in the absence of CR and a substantial contribution from the Eq. [1] iron term for most brain regions, the field dependence of brain ^1H_2O R_1 primarily arises from the B_0 dependence of r_{1M}. In other work involving in vivo ^2H-substitution titration rodent studies (44), we found that an increasing ^2H proportion increases ^1H_2O T_1 not only because the less competent ^2H replaces ^1H, but also because it induces cerebral edema and thus decreases f_M.

The magnetic field dependence of brain ^1H_2O longitudinal relaxation we observed is clearly non-Lorentzian (i.e., it deviates from the quadratic frequency dependence that would be expected if the relevant time correlation function were to decay exponentially). Non-Lorentzian behavior is typical of relaxation processes in microscopically heterogeneous systems. To more fully characterize the relaxation behavior so that various relaxation models could be properly evaluated would require increased sampling at low frequencies. For example, Korb and Bryant (45) presented elegant experiments on the field-dependent relaxation of water protons in protein solutions, and analyzed their data based on a two-site exchange system (protein–proton, water–proton) using a spin-phonon relaxation mechanism to couple the two spin systems. It is possible to conduct NMRD studies on phantom samples from a few

μT to several hundred mT (46). However, these techniques are not practical for human tissues in vivo. The modeling of in vivo human brain rotating-frame longitudinal relaxation rate constant ($R_{1\rho}$) data might provide access to these molecular dynamics. The $R_{1\rho}$ quantity is sensitive to fluctuations at very low frequencies—equivalent to B_0 values of a few μT (47).

ACKNOWLEDGMENTS

We gratefully acknowledge thoughtful discussions with Drs. Thomas Barbara (who suggested the power law transformation shown in Fig. 7b), Mark Wagshul, Jing-Huei Lee, and HaiFang Li. We thank Drs. Shalom Michaeli and Gregor Adriany for technical assistance, and Professors Joseph P. Hornak, Emanuel Kanal, and Ian R. Young for their help with Fig. 1a. W.D.R. and C.S.S. dedicate their efforts in this work to their mentor, colleague, and friend, the late Professor Harold L. Friedman.

REFERENCES

1. Freeman R, Robert JB. A brief history of high resolution NMR. NMR Basic Princ Prog 1990;25:1–15.
2. Vaughan JT, Garwood M, Collins CM, Liu W, DelaBarre L, Adriany G, Andersen P, Merkle H, Goebel R, Smith MB, Ugurbil K. 7T vs. 4T: RF power, homogeneity, and signal-to-noise comparison in head images. Magn Reson Med 2001;46:24–30.
3. Tkac I, Andersen P, Adriany G, Merkle H, Ugurbil K, Gruetter R. In vivo ^{1}H NMR spectroscopy of the human brain at 7T. Magn Reson Med 2001;46:451–456.
4. Koenig SH, Brown RD. Relaxometry of tissue. NMR Encycl 1996;6: 4108–4120.
5. Andrew ER, Bydder G, Griffiths J, Iles R, Styles P. Clinical magnetic resonance: imaging and spectroscopy. Chichester: John Wiley & Sons; 1980. p 36.
6. Ugurbil K, Garwood M, Ellermann J, Hendrich K, Hinke R, Hu X, Kim S-G, Menon R, Merkle H, Ogawa S, Salmi R. Imaging at high magnetic fields: initial experiences at 4T. Magn Reson Q 1993;4:259–277.
7. Fischer HW, Rinck PA, Van Haverbeke Y, Muller RN. Nuclear relaxation of human brain gray and white matter: analysis of field dependence and implications for MRI. Magn Reson Med 1990;16:317–334.
8. Venu K, Denisov VP, Halle B. Water ^{1}H magnetic relaxation dispersion in protein solutions. A quantitative assessment of internal hydration, proton exchange, and cross-relaxtion. J Am Chem Soc 1997;119:3122–3134.
9. Sammi MK, Felder CA, Fowler JS, Lee J-H, Levy AV, Li X, Logan J, Palyka I, Rooney WD, Volkow ND, Wang G-J, Springer CS. Intimate combination of low- and high-resolution image data: I. Real-space PET and ^1H_2O MRI, PETAMRI. Magn Reson Med 1999;42:345–360.
10. Rooney WD, Lee JH, Li X, Wang GJ, Franceschi D, Springer CS, Volkow ND. 4.0T water proton T_1 relaxation times in normal human brain and during acute ethanol intoxication. Alcohol Clin Exp Res 2000;24:830–836.
11. Rooney WD, Johnson G, Tanabe J, Li X, Lee J-H, Wagshul ME, Li H-F, Springer CS. Relaxometric relaxographic imaging of human brain. In: Proceedings of the 7th Annual Meeting of ISMRM, Philadelphia, PA, USA, 1999 (Abstract 609).
12. Labadie C, Lee J-H, Vetek G, Springer CS. Relaxographic imaging. J Magn Reson B 1994;105:99–112.
13. Silver MS, Joseph RI, Hoult DI. Selective spin inversion in nuclear magnetic resonance and coherent optics through an exact solution of the Bloch-Riccati equation. Phys Rev A 1985;31:2753–2755.
14. Friedman HL, Holz M, Hertz HG. EPR relaxations of aqueous Ni2 + ion. J Chem Phys 1979;70:3369–3383.
15. Kraft KA, Fatouros PP, Clarke GD, Kishore PR. An MRI phantom material for quantitative relaxometry. Magn Reson Med 1987;5:555–562.
16. Woods RP, Mazziotta JC, Cherry SR. MRI-PET registration with automated algorithm. J Comput Assist Tomogr 1993;17:536–546.
17. Bottomley PA, Foster TH, Argersinger RE, Pfeifer LH. A review of normal tissue hydrogen NMR relaxation times and relaxation mechanisms from 1–100 MHz: dependence on tissue type, NMR frequency, temperature, species, excision, and age. Med Phys 1984;11:425–448.
18. Lee JH, Li X, Sammi MK, Springer Jr CS. Using flow relaxography to elucidate flow relaxivity. J Magn Reson 1999;136:102–113.
19. Bryant RG, Marill K, Blackmore C, Francis C. Magnetic relaxation in blood and blood clots. Magn Reson Med 1990;13:133–144.
20. Hopkins AL, Yeung HN, Bratton CB. Multiple field strength in vivo T1 and T2 for cerebrospinal fluid protons. Magn Reson Med 1986;3:3003–3011.
21. Lacomis D, Osbakken M, Gross G. Spin-lattice relaxation (T1) times of cerebral white matter in multiple sclerosis. Magn Reson Med 1986;3: 194–202.
22. Miller DH, Johnson G, Tofts PS, MacManus D, McDonald WI. Precise relaxation time measurements of normal-appearing white matter in inflammatory central nervous system disease. Magn Reson Med 1989; 11:331–336.
23. Henderson E, McKinnon G, Lee TY, Rutt BK. A fast 3D Look-Locker method for volumetric T1 mapping. Magn Reson Imaging 1999;17: 1163–1171.
24. Kingsley PB, Ogg RJ, Reddick WE, Steen RG. Correction of errors caused by imperfect inversion pulses in MR imaging measurement of T1 relaxation times. Magn Reson Imaging 1998;16:1049–1055.
25. Steen RG, Reddick WE, Ogg RJ. More than meets the eye: significant regional heterogeneity in human cortical T1. Magn Reson Imaging 2000;18:361–368.
26. Gelman N, Ewing JR, Gorell JM, Spickler EM, Solomon EG. Interregional variation of longitudinal relaxation rates in human brain at 3.0T: relation to estimated iron and water contents. Magn Reson Med 2001; 45:71–79.
27. Wansapura JP, Holland SK, Dunn RS, Ball Jr WS. NMR relaxation times in the human brain at 3.0 Tesla. J Magn Reson Imaging 1999;9:531–538.
28. Jezzard P, Duewell S, Balaban RS. MR relaxation times in human brain: measurement at 4T. Radiology 1996;199:773–779.
29. Mason GF, Chu WJ, Hetherington HP. A general approach to error estimation and optimized experiment design, applied to multislice imaging of T1 in human brain at 4.1 T. J Magn Reson 1997;126:18–29.
30. Rooney WD, Li X, Springer CS, Telang FW, Coyle PK, Caparelli E, Ernst T, Chang L. Age and sex: effects on brain properties assessed by ^1H_2O T_1 histograms. In: Proceedings of the 11th Annual Meeting of ISMRM, Toronto, Canada, 2003 (Abstract 1087).
31. Li X, Rooney WD, Springer CS. A unified magnetic resonance imaging pharmacokinetic theory: Intravascular and extravascular contrast reagents. Magn Reson Med 2005;54:1351–1359.
32. Naruse S, Horikawa Y, Tanaka C, Hirakawa K, Nishikawa H, Yoshizaki K. Significance of proton relaxation time measurement in brain edema, cerebral infarction and brain tumors. Magn Reson Imaging 1986;4:293–304.
33. Kamman RL, Go KG, Berendsen HJ. Proton-nuclear magnetic resonance relaxation times in brain edema. Adv Neurol 1990;52:401–405.
34. Boisvert DPJ, Handa Y, Allen PS. Proton relaxation in acute and subacute ischemic brain edema. Adv Neurol 1990;52:407–413.
35. Fatouros PP, Marmarou A, Kraft KA, Inao S, Schwartz FP. In vivo brain water determination by T_1 measurements: effect of total water content, hydration fraction, and field strength. Magn Reson Med 1991;17:402–413.
36. Ogg RJ, Steen RG. Age-related changes in brain T_1 are correlated with iron concentration. Magn Reson Med 1998;40:749–753.
37. Hallgren B, Sourander P. The effect of age on non-haemin iron in the human brain. J Neurochem 1958;3:41–51.
38. Gossuin Y, Roch A, Muller RN, Gillis P. Relaxation induced by ferritin and ferritin-like magnetic particles: the role of proton exchange. Magn Reson Med 2000;43:237–243.
39. Randall LO. Chemical topography of the brain. J Biol Chem 1938;124: 481–488.
40. Aime S, Botta M, Fasano M, Terreno E. Lanthanide(III) chelates for NMR biomedical applications. Chem Soc Rev 1998;27:19–29.
41. Bolinger L, Cecil K, Englander S, Stolpen A. Comparison of breast imaging at 1.5T and 4.0T. In: Proceedings of the 6th Annual Meeting of ISMRM, Sydney, Australia, 1998 (Abstract 232).

42. Springer CS and Rooney WD. B_0-dependence of the CR-determined exchange regime for equilibrium transcytolemmal water transport: implications for bolus-tracking studies. In: Proceedings of the 9th Annual Meeting of ISMRM, Glasgow, Scotland, 2001 (Abstract 2241).
43. Rooney WD, Telang FW, Springer CS. Quantitative 4T determination of normal brain vascular properties suggests CR transport across BBB. In: Proceedings of the 10th Annual Meeting of ISMRM, Honolulu, HI, USA, 2002 (Abstract 1314).
44. Medina DC, Li X, Springer CS. Pharmaco-thermodynamics of deuterium-induced edema in living rat brain via ^1H_2O MRI: Implications for boron neutron capture therapy of malignant brain tumors. Phys Med Biol 2005;50:2127–2139.
45. Korb J-P, Bryant RG. Magnetic field dependence of proton spin-lattice relaxation times. Magn Reson Med 2002;48:21–26.
46. Lee SK, Moβle M, Myers W, Kelso N, Trabesinger AH, Pines A, Clarke J. SQUID-detected MRI at 132 μT with T_1-weighted contrast established at 10 μT–300 mT. Magn Reson Med 2005;53:9–14.
47. Michaeli S, Sorce DJ, Springer, CS, Ugurbil K, Garwood M. $T_{1\rho}$ MRI contrast in the human brain: modulation of the longitudinal rotating frame relaxation shutter-speed during an adiabatic RF pulse. J Magn Reson 2006;181:135–147.